The final publication is available at

https://doi.org/10.1016/j.apcatb.2018.12.034

Additional Information

CO₂ METHANATION CATALYZED BY ORIENTED MoS₂ NANOPLATELETS SUPPORTED ON FEW LAYERS GRAPHENE

Ana Primo[1], Jinbao He[1], Bogdan Jurca[2], Bogdan Cojocaru[2], Cristina Bucur[3], Vasile I. Parvulescu[2]* and Hermenegildo Garcia[2]*

[1] Instituto Universitario de Tecnología Química, Consejo Superior de Investigaciones Científicas-Universitat Politécnica de Valencia, Universitat Politecnica de Valencia, Av. De los Naranjos s/n, 46022 Valencia, Spain

[2] Department of Organic Chemistry, Biochemistry and Catalysis, Faculty of Chemistry, University of Bucharest, Bdul Regina Elisabeta 4-12, Bucharest 030016, Romania

[3] National Institute of Materials Physics, Str. Atomistilor 405A, POBox MG7, 077125 Magurele, Romania.

Abstract.

Powders of molybdenum disulfide platelets strongly grafted on graphene have been prepared by pyrolysis of ammonium alginate containing adsorbed various proportions of $(NH_4)_2MoS_4$. After pyrolysis, formation of MoS_2 supported on graphene was determined by XRD and electron microscopy and spectroscopic techniques. MoS_2/G exhibits catalytic activity for the methanation of CO_2, the performance being optimal at intermediate loadings. The catalytic activity of sharply contrasts with that of bulk MoS_2 that promotes the reverse water gas shift, affording CO as the main product. Characterization of the spent MoS_2/G catalyst shows the partial conversion of external MoS2 into MoO3. Comparison of the catalytic activity of MoS_2/G with that of MoO_3/G shows that the latter is less efficient, but more selective for CO_2 methanation.

Introduction

In the context of diminishing atmospheric CO_2 emissions, one of the possibilities is utilization of CO_2 as feedstock for the production of fuels and other chemicals.[1-4] Hydrogenation is among the few CO_2 transformations that are thermodynamically downhill and this reaction renders products that can be used as fuels or bulk chemicals.[5,6] The hydrogen required in this process is expected be available in large amounts from water electrolysis using renewable electricity.[7-9] In view of this future scenario, there is a large incentive in developing non-noble metal catalysts to perform CO_2 hydrogenation forming products with high selectivity and efficiency at adequate rates under suitable conditions.[10,11]

Molybdenum oxides and chalcogenides have been proposed as alternative catalysts to platinum for a series of reactions, including hydrogen evolution in electrolysis, hydrodesulfuration and synthesis gas conversions.[12-16] All these reactions have in common hydrogen as the reaction product or reagent. The use of molybdenum disulfide supported on graphene for electrocatalytic hydrogen evolution has been considered a breakthrough in this area, since this composite material can exhibit catalytic performance close

to that of Pt nanoparticles due to the combination of the electrical conductivity of graphenes and the catalytic activity of MoS_2.[17,18]

Molybdenum has also been investigated for the valorization of CO_2. Early in 1981, Saito and Anderson [19] studied the activity of a series of molybdenum compounds for the methanation of CO_2 including oxides, sulfide, metal, carbide, and nitride, showing much higher reaction rates for MoO_2 than for Mo sulphides. While iron deactivated rapidly, molybdenum produced hydrocarbons in a certain extent and catalyzed the water gas-shift reaction. It was also demonstrated that in the presence of molybdenum, coke is not formed due to the efficient hydrogenation of the carbonaceous deposits.[20] On the other hand, MoS_2 has been used as support of Pt nanoparticles in the hydrogenation of CO_2, mainly to methanol.[21]

Density functional theory (DFT) employed to investigate the methanol synthesis from CO_2 and H_2 on a Mo_6S_8 cluster (the structural building block of the Chevrel phase of molybdenum sulfide) indicated that MoS_2 can promote the C−O scission of H_xCO intermediates, thus explaining the high selectivity of molybdenum sulfides for the production of hydrocarbons. In contrast, the Mo_6S_8 cluster is predicted to have moderate activity for converting CO_2 and H_2 to methanol. Both the Mo and S sites participate in the reaction with CO_2, CO, and CH_xO, being Mo preferentially the binding sites, whereas S atoms facilitate H−H bond cleavage by forming relatively strong S−H bonds. The unexpected activity of the Mo_6S_8 cluster was considered to be the result of the interplay between shifts in the Mo d-band and S p-band in a unique cage-like geometry.[22] The catalytic activity of MoS_2 surface for CO hydrogenation has also been studied by DFT and calculations suggest that the active sites correspond to edge Mo atoms adsorbing CO.[23]

The association of molybdenum with carbon has also been indicated as beneficial by both experimental results and theoretical calculations. Thus, Cu-Mo_2C/MCM-41 was tested for CO_2 hydrogenation to form methanol. The activity of this catalyst was associated to a strong synergistic effect between Cu and Mo_2C, which also resulted in a higher selectivity for methanol.[24] Au and Cu, were also associated to molybdenum carbide (Au/δ-MoC and Cu/δ-MoC) catalysts affording high activity, selectivity, and stability for the reduction of CO_2 to CO with some subsequent selective hydrogenation toward methanol. A detailed comparison of the behavior of Au/β-Mo_2C and Au/δ-MoC catalysts also based on sophisticated experiments under controlled conditions and DFT calculations provided evidence of the impact of the metal/carbon ratio in the carbide on the performance of the catalysts.[25] DFT calculations also differentiate between the Mo_2C(001) and Mo_2C(101) surfaces, the latter affording an effective barrier allowing the surface C hydrogenation on the Mo_2C(101) surface activated by the presence of 2O and 2OH pre-covered surfaces.[26] The reverse water–gas shift reaction is also catalyzed by potassium-promoted molybdenum carbide supported on γ-Al_2O_3 (K-Mo_2C/γ-Al_2O_3).[27] DFT calculations have also been carried out for two-dimensional transition-metal carbides as CO_2 conversion catalysts. Among these Mo_3C_2 was found to exhibit a very promising CO_2 to CH_4 selective conversion capability. Calculations predicted the formation of OCHO$^•$ and HOCO$^•$ radical species in the early hydrogenation steps through spontaneous reactions.[28]

Continuing with the use of molybdenum disulfide supported on graphene as catalyst, we have reported recently the preparation in one step of samples of few layers MoS_2 platelets supported on few-layers graphene (MoS_2/G) by pyrolysis at 900 °C under inert atmosphere of natural polysaccharides containing ammonium molybdotetrasulfide.[29] In this process a spontaneous segregation of graphene and MoS_2 takes places during the thermal restructuring of the polysaccharide forming graphene and carbochemical reduction of $(NH_4)_2MoS_4$ becoming precursor of MoS_2. The resulting MoS_2/G is a photocatalyst for hydrogen generation from water in the presence of sacrificial electron donors and using Eosin Y as photosensitizer and also for the electrocatalytic H_2 evolution reaction.[29] Further characterization when the MoS_2/G heterojunction is prepared as film has revealed that the MoS_2 nanoplatelets with lateral dimensions between 15 and 105 nm and height between 5 and 15 nm, depending on MoS_2 loading, are preferentially oriented in the 0.0.2 crystallographic facet.[30] This preferential orientation is proposed to derive from the lattice matching of this MoS_2 crystallographic facet with the graphene hexagonal arrangement.

Aimed at expanding the scope of MoS_2/G as catalyst and considering the above-commented interest in CO_2 hydrogenation and reports on the molybdenum catalysts, the present manuscript reports the catalytic activity of MoS_2/G for CO_2 methanation, comparing the performance of MoS_2/G with that of analogous MoO_3/G samples, prepared by impregnation of preformed MoO_3 nanoparticles on G. It will be shown that MoS2/G is efficient in promoting the selective CO_2 methanation, but it undergoes a gradual deactivation attributable to the conversion of MoS_2 to MoO_3 that, although still active, is less efficient than the fresh disulfide.

Experimental section

Synthesis of MoS$_2$/G samples

Different amounts of $(NH_4)_2MoS_4$ (560, 280, 140, and 70 mg for the samples MoS_2/G 2:1, 3:1, 4:1 and 5:1, respectively) were dissolved in 10 ml of water. Then, 1.00 g of alginic acid is dissolved in the same solution with 0.5 ml of NH_4OH. When the mixture is well dissolved, the water is evaporated under reduced pressure and the resulting solid is pyrolysed under argon flow at 250 °C for 2 h and, then, at 900 °C for 2 h (5 °C min^{-1} heating rate). After pyrolysis, the powder is ground and exfoliated in water using a 750 W Sonics Vibracell high intensity ultrasonic liquid processor for 1.5 h.

Synthesis of MoO$_3$/G samples

Alginic acid is pyrolyzed under argon flow at 250 °C for 2 h and, then, at 900 °C for 2 h (5°C min^{-1} heating rate). 300 mg of the obtained carbonaceous residue is exfoliated in 300 mL of water using a 750 W Sonics Vibracell high intensity ultrasonic liquid processor for 1.5 h. Also, different amounts of commercial MoO_3

(15, 90 and 180 mg for the samples MoO$_3$-1/G, MoO$_3$-2/G and MoO$_3$-3/G, respectively) were sonicated in the same manner. Afterwards, the two suspensions were mixed and submitted to further sonication for 1.5 h. Then, the solid is filtered and washed with 1 L of deionized water and, finally, dried under vacuum overnight.

Catalytic tests and kinetics

Catalytic tests were performed in a setup (Microactivity tester, PID Eng&Tech) equipped with a stainless steel (316 SS) fixed bed tube reactor (Autoclave Engineers) featured with an inner K-type thermocouple. Two mass flow controllers (EL-FLOW Select, Bronkhorst) were used to feed the mixture of the inlet gases: hydrogen (5.0, Linde) and carbon dioxide (4.5, Linde). The total gas flow rate was checked before each experiment by help of a gas burette connected to the outlet of the reactor setup. An amount of 20 mg catalyst powder was introduced in the reactor; air was removed by flushing the system at room temperature for 15 min with 30 mL/min H$_2$ and 10 mL/min CO$_2$, followed by 30 min catalytic reaction at the flow rates of 3 mL/min H$_2$ and 1 mL/min CO$_2$. Afterwards, the reactor was pressurized at 10 bar. Five reaction temperatures between 300 and 500 °C were investigated. For each temperature, a set of three successive GC analyses were performed (at 5, 25 and 45 minutes after the stabilization of the temperature). The values of the CO$_2$ conversion obtained from the last two GC measurements coincided very well in all the experiments, indicating that the reactor setup reached the steady state operation conditions.

GC analyses were performed using H$_2$ as carrier gas on an Agilent 7890A chromatograph equipped with a capillary PLOT column (RT-Msieve 5A, Restek) and a TCD detector. Temperature program considered a 5 min dwell at 50 oC, a ramp with 25 °/min to 250 °C followed by a final dwell of 5 min, allowing thus a very good separation between CH$_4$, CO and CO$_2$. The gas samples were injected through a remotely controlled 6-way valve (A4C6WE, Vici) kept at ambient temperature. The reproducibility of the analysis system was checked prior to each experiment by injecting a series of three successive samples of gas mixture passed through the reactor at room temperature.

Estimation of the diffusion coefficients:

The reaction mixture has been treated as a pentacomponent (CO$_2$, H$_2$, CH$_4$, CO, H$_2$O) real gas. The diffusion coefficient D_{im} of each component i in the gas mixture was estimated from the binary diffusion coefficients using Blanc's law (1):

$$D_{\mathrm{im}} = \left(\sum_{i=1, j \neq i}^{n} \frac{x_j}{D_{\mathrm{ij}}} \right)^{-1} \tag{1}$$

where:

D_{im}= diffusion coefficient of the component (i) in the gas mixture (m)

x_j = mole fraction of the component j

D_{ij} = binary diffusion coefficients for each ij components pair

      Each D_{ij} coefficient was further estimated from Chapman-Enskog formula (2) or its Wilke-Lee modification (3):

$$D_{12} = \frac{0.00266 T^{3/2}}{P M_{12}^{1/2} \sigma_{12}^2 \Omega_D} \tag{2}$$

$$D_{12} = \frac{\left[3.03 - \left(0.98/M_{12}^{1/2}\right)\right]\left(10^{-3}\right)T^{3/2}}{P M_{12}^{1/2} \sigma_{12}^2 \Omega_D} \tag{3}$$

where:

D_{12} - binary diffusion coefficient, cm^2/s

T - absolute temperature, K

$M_{12} = 2\left(\frac{1}{M_1} + \frac{1}{M_2}\right)^{-1}$; M_1, M_2 - molecular weights of components 1 and 2, g/mol

P - pressure, bar

$\sigma_{12} = (\sigma_1 + \sigma_2)/2$ - characteristic length (*i.e.* kinetic diameter) for binary collision between molecules of the components 1 and 2, Å

Ω_D - diffusion collision integral, dimensionless

      The value of the collision integral Ω_D depends on the energy of intermolecular interactions which is commonly described by a 6-12 Lennard-Jones potential that depends on the characteristic length σ_{12} and the depth of the energy well ε. Tabulated data of σ_i(Å) and $\varepsilon_i/k_{Boltzmann}$ (K) [31] for pure components were used to calculate $\sigma_{ij, i \neq j}$ (as arithmetic mean between σ_i and σ_j) and $\varepsilon_{ij, i \neq j}/k_B$ (as geometric mean between ε_i/k_B and ε_j/k_B); the last allows the calculation of the corresponding Ω_D integral using Neufield parametrization [31]:

$$\Omega_D = \frac{A}{(T^*)^B} + \frac{C}{e^{DT^*}} + \frac{E}{e^{FT^*}} + \frac{G}{e^{HT^*}} \tag{4}$$

where: $T^* = k_B T/\varepsilon_{ij}$; A=1.06036 ; B=0.1561 ; C=0.193; D=0.47635; E=1.03587 ; F=1.52996; G=1.76474 ; H=3.89411

      The consistency of the parameterizations used in Chapman-Enskog and Wilke-Lee estimation methods was checked by calculating values of binary D_{12} coefficients (0°C, 1 atm) and comparing the obtained values with experimental results [32]:

Calculation of the Weisz-Prater number:

The adimensional Weisz-Prater criterion [33,34] is given by:

$$N_{W-P} = \frac{r\rho_{cat}R_p^2}{C_s D_{eff}} \leq 0.3 \qquad (5)$$

where:

r - reaction rate expressed per unit mass of catalyst, $mol \cdot s^{-1} \cdot (g^{-1})_{cat}$

ρ_{cat} - packed catalyst density, $g \cdot cm^{-3}$

R_p - catalyst particle radius, cm

C_s - concentration of the reactant at the surface of the catalyst particles, $mol \cdot cm^{-3}$

D_{eff} - effective diffusion coefficient, $cm^2 \cdot s^{-1}$
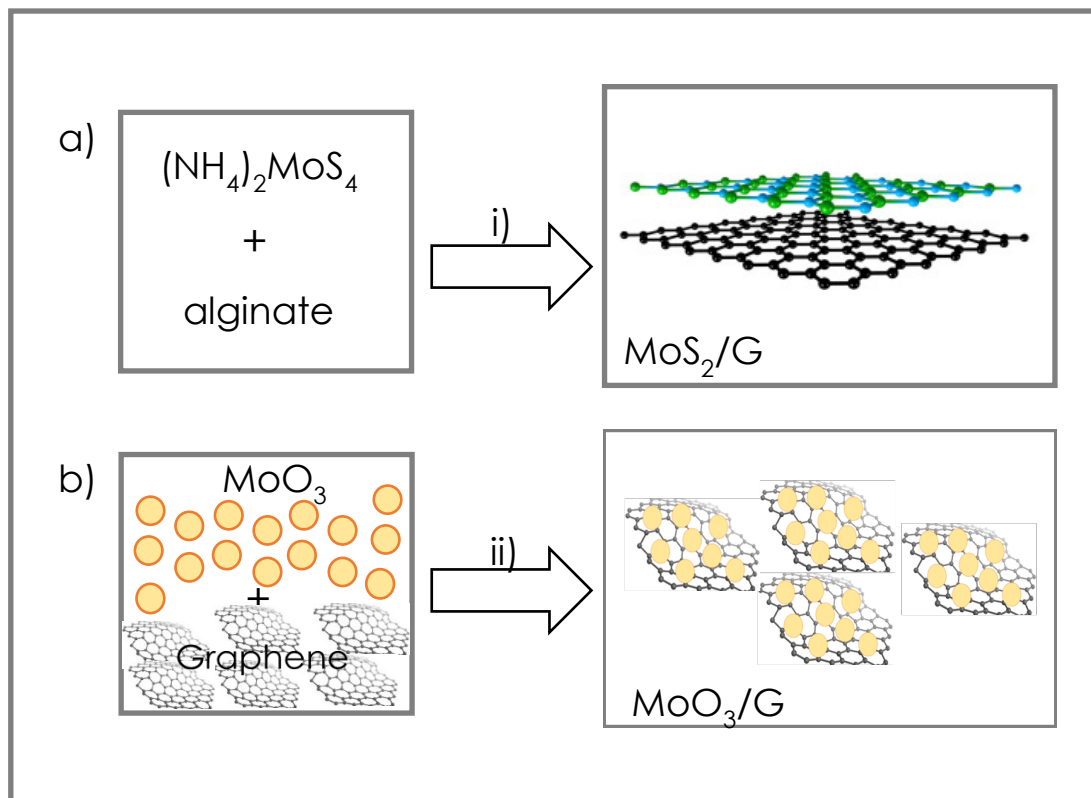
Characterization techniques

The Raman measurements (Horiba JobinYvon – Labram HR UV–Visible–NIR 200–1600 nm Raman Microscope Spectrometer) were carried out at room temperature with the 633 nm line of a He-Ne ion laser as excitation source. XRD patterns were obtained in a Philips XPert diffractometer (40 kV and 45 mA) equipped with a graphite monochromator employing Ni-filtered Cu Kα radiation (1.541178 Å). AFM images were made with a Multimode Nanoscope 3A equipment working in tapping mode, using mica as substrate. FESEM images were taken with an ULTRA 55 ZEISS Oxford instrument and HRTEM images with a JEM 2100F JEOL 200 kV electronic microscope.

Results and Discussion.

Sample preparation and characterization

Two types of materials, either MoS_2/G or MoO_3/G were prepared in the present study to be tested as CO_2 hydrogenation catalysts. Scheme 1 illustrates the preparation procedure followed for each type of sample under study, while Table 1 summarizes relevant composition data and average particle size. As it can be seen there, the MoS_2/G samples were prepared by pyrolysis at 900 °C of alginate containing different amounts of $(NH_4)_2MoS_4$ adsorbed on the fibrils. This preparation procedure was previously reported and it was found that under pyrolysis conditions, alginate is converted into a turbostratic graphitic carbon that upon exfoliation disperses into defective graphene with a residual oxygen content about 8 %.[35,36] On the other hand, $(NH_4)_2MoS_4$ undergoes transformation into MoS_2, occurring a spontaneous phase segregation under the conditions of the thermal treatment.[29,30] The strong grafting between the MoS_2 and the defective graphene phase is manifested by the 002 facet orientation and nanoplatelet morphology of the MoS_2 nanoparticles wetting the graphene sheets.

Scheme 1. Pictorial illustration for the preparation of a) MoS_2/G and b) MoO_3/G.

Table 1. List of samples prepared in the present study, relevant composition data and average particle.

Sample	MoS_2 or MoO_3 (wt%)	Particle size (nm)
G	--	--
MoS_2-1/G	0.9	200-350
MoS_2-2/G	2.4	200-350
MoS_2-3/G	4.2	200-400
MoS_2-4/G	12.7	250-400
MoO_3-1/G	0.54	14.96
MoO_3-2/G	6.24	22.86
MoO_3-3/G	11.23	40.69

Three MoS_2/G samples containing different proportions of $(NH_4)_2MoS_4$ were prepared in order to determine the influence of MoS_2 content on the catalytic performance. Table 1 summarizes the MoS_2 content of the three MoS_2/G samples. It has been observed that MoS_2 loading determines the average size

of MoS$_2$ nanoplatelets[30] and this parameter exerts generally a strong influence on the catalytic activity of the materials.

Characterization data of MoS$_2$/G was in agreement with the literature. In particular, XRD patterns shown in Figure S7 were in agreement with the formation of MoS$_2$ from (NH$_4$)$_2$MoS$_4$ during the pyrolysis, exhibiting a preferential orientation in the 002 facet, as reported.[30] This preferential orientation is reflected in the XRD pattern of the MoS$_2$/G by the presence of a strong peak corresponding to the diffraction in these 002 planes and the absence or negligible intensity of the diffraction in other crystallographic planes. In addition, Raman spectroscopy presents the three 2D, G and D peaks typical for defective G appearing at about 2750, 1590 and 1350 cm^{-1}, respectively. In addition, in the low frequency range, the E$_g$ and A$_{2g}$ vibrations due to the MoS$_2$ appearing about 410 and 380 cm^{-1} were also recorded. Raman spectra will be further commented latter when discussing MoS$_2$/G stability under reaction conditions.

SEM images of the MoS$_2$/G samples show that before exfoliation the material is constituted by an ensemble of thin platelets, while after sonication TEM images reveal the expected layered morphology for G of about 1-2 μm of lateral size with low contrast, on top of which the presence of smaller MoS$_2$ particles of lateral dimensions between 200 to 400 nm can be observed. Higher resolution of the MoS$_2$ particles shows the presence of few layers, in agreement with MoS$_2$ structure. Measurements of the interplanar distance in these nanoplatelets gives a value of 0.63 nm that is in agreement with the expected 002 interplanar distance of MoS$_2$ according to the data in the literature.[37] Figure 1 presents a selection of SEM and TEM images to illustrate the morphology of the MoS$_2$/G catalyst.
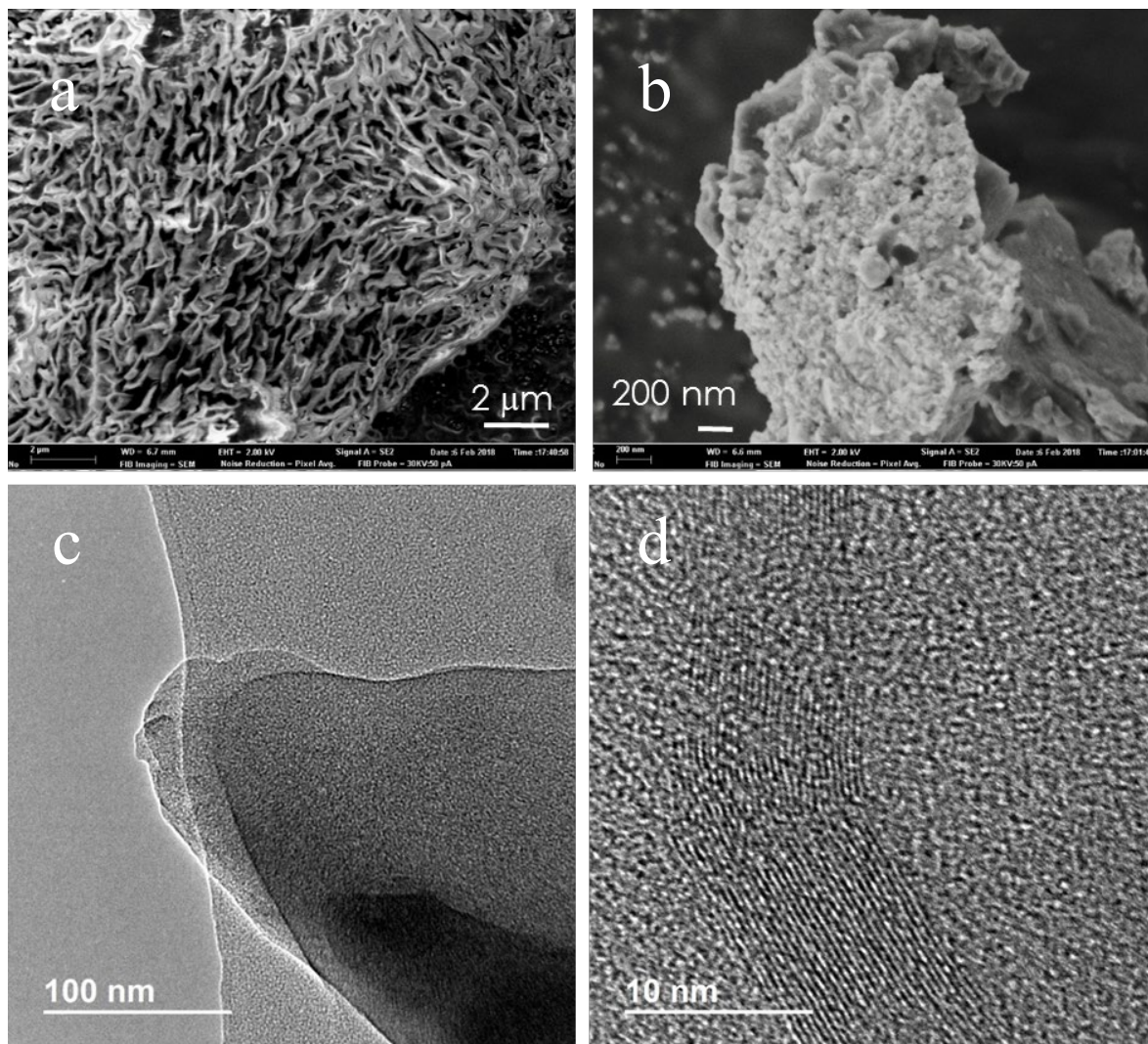
Figure 1. Images of SEM (a and b) before sonication and TEM (c and d) after sonication corresponding to the MoS$_2$/G catalyst with the lowest MoS$_2$ loading.

The identity of the different particles, particularly the MoS$_2$ nanoplatelets, was firmly supported by EDX analysis that established the presence of Mo and S in these platelets with the expected 1.2 stoichiometry.

Preparation of the MoO$_3$/G samples is also illustrated in Scheme 1, while Table 1 contains relevant characterization data. In this case, the samples were obtained by adsorbing commercial MoO$_3$ nanoparticles on graphene previously obtained by pyrolysis of alginate and subsequent exfoliation by sonication.[35] Adsorption was carried out by suspending in water MoO$_3$ and graphene under continuous sonication, recovering the sample by filtration. Finally, MoO$_3$/G was exhaustively washed to remove weakly adsorbed nanoparticles. The maximum temperature at which MoO$_3$/G sample was submitted was 100 °C. Worth noting is that the particle size of MoO$_3$ is significantly smaller than that of MoS$_2$, what should favor the activity of MoO$_3$ over that of MoS$_2$. As in the previous case of MoS$_2$/G, three different samples containing increasing loadings of MoO$_3$ were prepared. The presence of MoO$_3$ on the graphene samples was assessed by XRD and by TEM images. Figure 2 shows selected TEM images corresponding to the MoO$_3$/G sample at

intermediate loading (6.2 wt%) were the presence of MoO_3 nanoparticles with average particle size about 22.8 nm was clearly observed on top of graphene sheet. It was noted that the average MoO_3 particle size increases with the MoO_3 content from about 15 to 40 nm, reflecting the occurrence of agglomeration of the primary nanoparticles as the percentage of MoO_3 increases. The MoO_3 loading was determined by ICP chemical analysis of the MoO_3 content, ranging from 0.5 to 11 %.
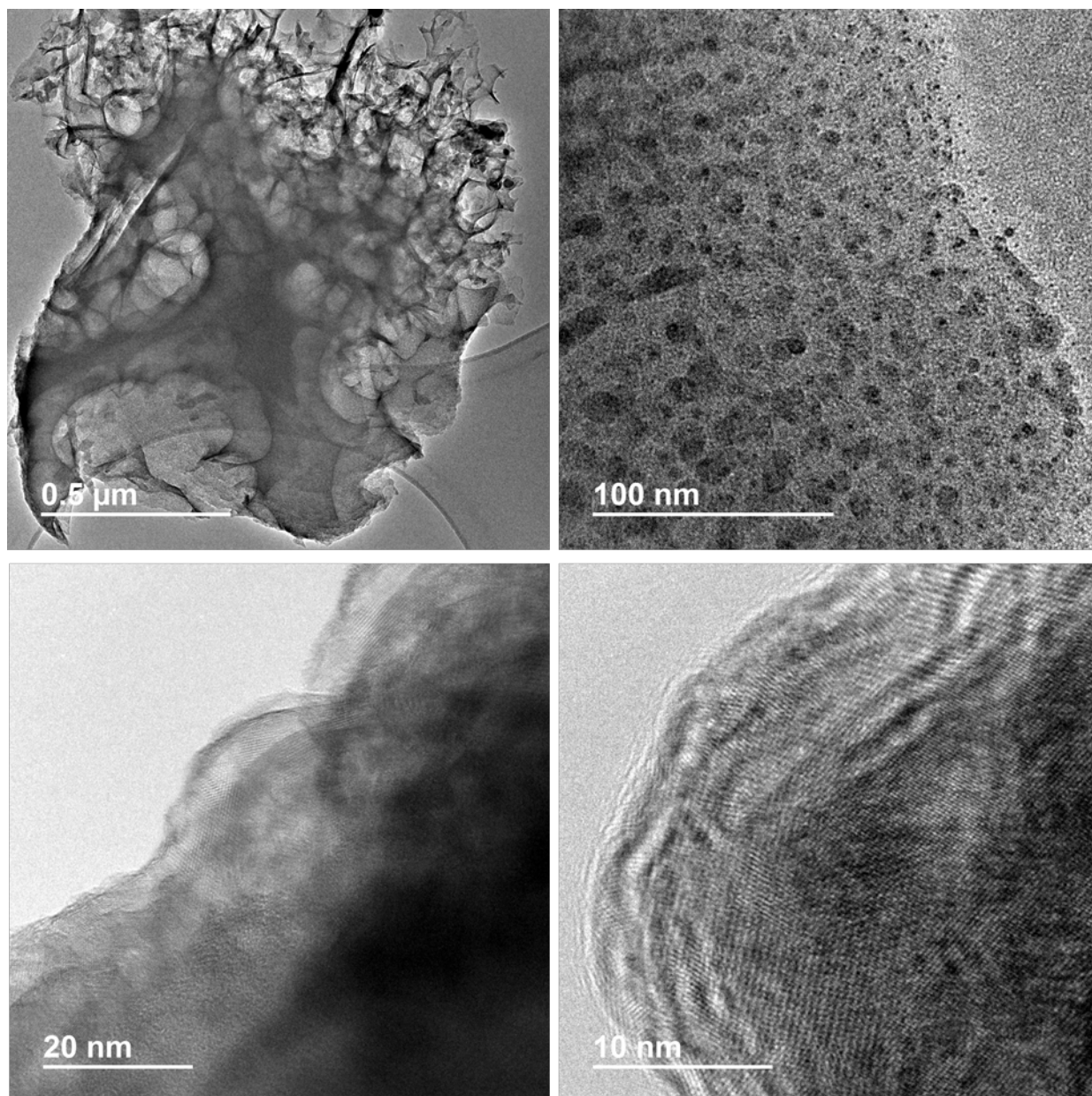

Fig.2 Top: TEM images of MoO_3-2/G at different magnifications. Bottom: TEM images of G used to adsorb MoO_3 NPs.

Catalytic tests.

As commented in the introduction, the purpose of the present study is to assess the catalytic activity of graphene supported Mo samples for CO_2 hydrogenation. A summary of the results for the set of samples at different reaction temperatures is presented in Table 1 and Figure 3. As it can be seen there, in the range

of temperatures under study from 250 to 500 °C, conversion of CO_2 increase with the reaction temperature, indicating that conversion at the experimental conditions is under kinetic control.
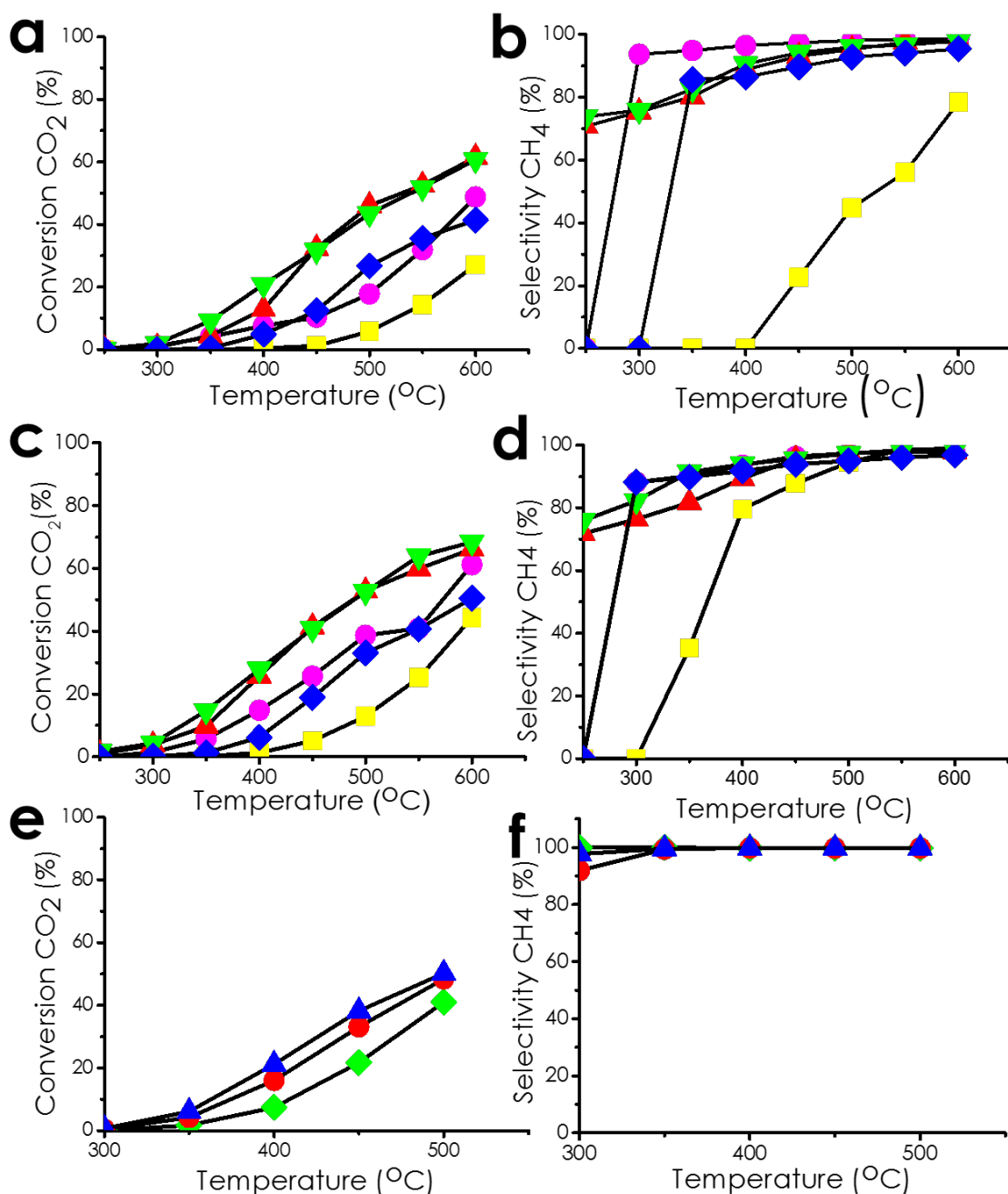

Figure 3. Conversion (a, c and e) and methane selectivity (b, d and f) plots for CO_2 hydrogenation as a function of the temperature promoted by MoS_2/G or MoO_3/G catalysts as a function of loading. Legends: ■) G; ●) MoS_2-1/G; ▲) MoS_2-2/G ▼) MoS_2-3/G ◇) MoS_2-4/G. Reaction conditions for **a** and **b**: P=10 bar, Flow rates: H_2: 15 mL/min and CO_2: 5 mL/min, catalyst amount: 20 mg; Reaction conditions for **c** and **d**: Flow rates: H_2: 3 mL/min; CO_2: 1 mL/min Catalyst amount: 20 mg. Legends for plots **e** and **f)** ♦) MoO_3-1/G ; ●) MoO_3-2:G; ▲) MoO_3-3:G. Reaction conditions: P=10 bar Flow rates: H_2: 3 mL/min; CO_2: 1 mL/min Catalyst amount: 20 mg.

Blank controls in the absence of any catalyst shows that negligible CO_2 conversions occur in the absence of any catalyst in the range of temperatures under study. The two products detected in all the experiments were methane and CO. When the reaction was carried out with graphene in the absence of Mo or with MoS_2 in the absence of graphene, CO was the major product, while for the MOS_2/G and MO_3/G samples under study the major product was methane, frequently with selectivity above 95 % and in some cases close to 100 %. Thus, another control using as catalyst graphene, in the absence of any MoS_2 or MoO_3, also indicates a low conversion (about 6 %) at the highest temperature under study, with a product distribution different to those when Mo compounds are present. It appears that graphene support exhibits some catalytic activity, in accordance with the known activity of graphene as metal-free hydrogenation catalyst of alkenes and nitro groups, among others.[38-40] It seems, however, that under the present conditions its contribution to CO_2 conversion is minor compared to that of Mo species that appear to be the active sites of CO_2 hydrogenation. The catalytic activity of bulk MoS_2 in the absence of graphene was also checked, observing a significant CO_2 conversion over 30 % with almost complete selectivity towards CO. The results are compiled in Table S2 of the supporting information. This selectivity towards CO sharply contrasts with that observed for the defective graphene supported Mo samples indicated in Table 1, for which CH_4 was the major product. This comparison between bulk MoS_2 and facet oriented MoS_2/G clearly reveals the role of strong support-MoS_2 interaction with defective graphene altering the reaction mechanism and determining a drastic change in product selectivity.

An influence of the Mo content on the catalytic activity was clearly observed. In the case of MoO_3/G, the catalytic activity increases along the Mo content, although not linearly. Thus, it was observed that the most active MoO_3/G sample was the one containing the highest MoO_3 content. However, the MoO_3/G sample with the MoO_3 loading as low as 0.5 % was the one that exhibits the highest TOF values, indicating that the activity per Mo atom decreases upon loading increase. For these MoO_3 samples, CH_4 selectivity was above 99 % except for reactions at 300 °C, for which CO was detected in somewhat higher selectivity, but always below 10 %. Figure S5 shows the variation of the Gibbs free energy with temperature for the hydrogenation of CO_2 for different H_2/CO_2 ratios. According to these variations a higher H_2/CO_2 ratio makes the reaction more favorable also favoring an increase in the selectivity to methane. The production of CO is favored at high temperatures. For the H_2/CO_2 ratio of 3 considered in our experiments the thermodynamic differences allows the production of both the CO and methane. Therefore, the difference in the selectivity is controlled by the catalyst and values measured for graphene, very different to those MoO_3/G samples, account for this.

In contrast to the case of MoO_3/G, the performance of MoS_2/G as a function of the MoS_2 content exhibits a volcano plot, there being an optimal amount of MoS_2 to achieve the highest CO_2 conversion between 25 and 33 %, conversion decreasing as MoS_2 loading increases or decreases with respect to this range. This optimal loading is probably due to the compromise between two opposite factors influencing

the catalytic performance. On one hand, the number of active sites due to MoS_2 should increase with loading, but, on the other hand, as previously discussed, particle size also increases with loading. For this reason a balance between small particle size and number of sites is reached at intermediate MoS_2 loading. With regard to selectivity to methane, it was observed that methane selectivity for MoS_2/G was significantly lower than the values for MoO_3/G, and particularly at low temperatures and low CO_2 conversions, CO selectivities over 10 % were measured. This is again the effect of a kinetic controlled effect.

The deposition of MoS_2 and MoO_3 onto graphene changed the previously reported order of the activity,[19] MoS_2 being more active. However, the methanation was almost complete on MoO_3/G compared to MoS_2/G on which part of the CO_2 was reduced only to CO.

Table 2 compiles values of the Weisz-Prater criterion for differential reaction conditions (CO_2 conversion < 5%, P=10 bar, CO_2:H_2 (vol) = 1:3). The values inside demonstrate a very good agreement between Chapman-Enskog (C-E) and Wilkee-Lee (W-L) approaches and experimental results. Thus, for $D_{CO2\text{-}H2}$ C-E: 0.531, W-L: 0.505, and exp.: 0.55 cm^2/s, and for $D_{CO2\text{-}CH4}$ C-E: 0.141, W-L: 0.150, and exp.: 0.153 cm^2/s). The values of the diffusion coefficients for the reactants in the gas reaction mixture ($D_{CO2,m}$ and $D_{H2,m}$) calculated using Blanc's law are presented in the same Table 2.

The reaction rate was calculated for differential reaction conditions (CO_2 conversion < 5%) where, for low X_i values, the formula (6) of the conversion rate in a packed-bed plug flow reactor (PFR) [41] becomes approximately equal to (7) that describes the mass balance of a continuous tank stirred reactor (CSTR), allowing thus a simple calculation of CO_2 consumption rates ($\overline{-r_i}$) listed in Table 2. The high selectivity values in CH_4 indicate that the prevalent occurring reaction is $CO_2 + 4H_2 = CH_4 + 2H_2O$ and, thus, the consumption rate of H_2 has been approximated as four times the consumption rate of CO_2.

$$\frac{m_L}{(F_0)_i} = \int_0^{X_A} \frac{dX_i}{-r_i} \qquad (6)$$

$$\frac{m_L}{(F_0)_i} = \frac{X_i}{\overline{-r_i}} \qquad (7)$$

where:

m_L = mass of catalyst, g

F_0 = molar flow rate, mol/s

X_i = fractional conversion of reactant i

r_i = molar rate of reactant i consumption, per unit mass of catalyst, mol/(s·g)

$\overline{-r_i}$ = average specific rate of reactant i consumption in the conversion range [0, X_i] Particle radii and bulk catalyst densities are: MoS_2-1/G - 1.375·10^{-5} cm; 0.289 g·cm^{-3}, MoS_2-2/G - 1.5·10^{-5} ; 0.247 , MoS_2-3/G - 1.5·10^{-5} ; 0.276 , MoS_2-4/G - 1.75·10^{-5} ; 0.337 , MoO_3-1/G - 0.75·10^{-6} ; 0.233 , MoO_3-2/G - 1.15·10^{-6} ; 0.256 , MoO_3-3/G - 2.05·10^{-6} ; 0.310.

The concentration of the reactants at the surface of the catalyst has been considered the same as in the gas mixture due to the low values of the space velocities and pressure/temperature values used during the experiments. Critical parameters were used to determine the *a* and *b* Van der Waals constants of pure gases that were summed according to the mixing rules described by Hirschfelder et al. [31] to obtain the *a* and *b* constants of the pentacomponent gas reaction mixtures. The molar volume was further calculated from the Van der Waals equation of state. Slightly larger values compared to the application of the ideal gas equation of state were determined indicating thus a very small prevalence of the repulsive inter-molecular forces. The ratio between the mole fraction of the reactant and the molar volume allows to the reactant concentrations listed in Table 2.

Very important to notice, all values of the Weisz-Prater criterion calculated for the experiments occurring in differential reactions conditions (Table 2) are by far smaller than 0.3 indicating that no mass transfer limitations affect the ongoing catalytic reactions.

Table 2: Values of the Weisz-Prater criterion for differential reaction conditions (CO_2 conversion < 5%), P=10 bar, CO_2:H_2 (vol) = 1:3.

Catalyst	T (^{O}C)	Total flow (mL/min)	C_{CO2} (mol/cm^3)	C_{H2} (mol/cm^3)	$D_{CO2,m}$ (cm^2/s)	$D_{H2,m}$ (cm^2/s)	$\overline{-r_{CO_2}}$ mol/(s·g$_{cat}$)	N_{W-P} CO_2	N_{W-P} H_2
MoS$_2$-1/G	300	4	5.24·10^{-5}	1.57·10^{-4}	0.253	0.759	1.12·10^{-7}	4.61·10^{-13}	2.05·10^{-13}
	300	20	5.18·10^{-5}	1.55·10^{-4}	0.241	0.734	4.09·10^{-6}	1.79·10^{-11}	7.88·10^{-12}
	350	4	4.70·10^{-5}	1.39·10^{-4}	0.260	0.802	1.86·10^{-6}	8.30·10^{-12}	3.65·10^{-12}
	350	20	4.76·10^{-5}	1.42·10^{-4}	0.277	0.844	4.28·10^{-6}	1.76·10^{-11}	7.78·10^{-12}
MoS$_2$-2/G	300	4	5.12·10^{-5}	1.53·10^{-4}	0.233	0.718	1.41·10^{-6}	6.59·10^{-12}	2.86·10^{-12}
	300	20	5.22·10^{-5}	1.56·10^{-4}	0.249	0.753	1.54·10^{-6}	6.59·10^{-12}	2.91·10^{-12}
	350	20	4.70·10^{-5}	1.40·10^{-4}	0.265	0.817	8.13·10^{-6}	3.63·10^{-11}	1.58·10^{-11}
MoS$_2$-3/G	300	4	5.14·10^{-5}	1.53·10^{-4}	0.235	0.722	1.23·10^{-6}	6.31·10^{-12}	2.75·10^{-12}
	300	20	5.17·10^{-5}	1.54·10^{-4}	0.240	0.733	4.65·10^{-6}	2.33·10^{-11}	1.02·10^{-11}
MoS$_2$-4/G	350	20	4.79·10^{-5}	1.43·10^{-4}	0.283	0.856	2.79·10^{-6}	2.13·10^{-11}	9.42·10^{-12}
	400	20	4.35·10^{-5}	1.29·10^{-4}	0.298	0.919	9.11·10^{-6}	7.26·10^{-11}	3.19·10^{-11}
MoO$_3$-1/G	300	4	5.24·10^{-5}	1.57·10^{-4}	0.254	0.762	2.60·10^{-8}	2.57·10^{-16}	1.14·10^{-16}
	350	4	4.78·10^{-5}	1.43·10^{-4}	0.281	0.852	6.32·10^{-7}	6.18·10^{-15}	2.73·10^{-15}
MoO$_3$-2/G	300	4	5.23·10^{-5}	1.57·10^{-4}	0.252	0.758	1.48·10^{-7}	3.83·10^{-15}	1.70·10^{-15}
	350	4	4.72·10^{-5}	1.40·10^{-4}	0.265	0.814	1.56·10^{-6}	4.24·10^{-14}	1.87·10^{-14}
MoO$_3$-3/G	300	4	5.23·10^{-5}	1.56·10^{-4}	0.250	0.753	2.60·10^{-7}	2.59·10^{-14}	1.49·10^{-14}
	350	4	4.67·10^{-5}	1.37·10^{-4}	0.254	0.787	2.27·10^{-6}	2.49·10^{-13}	1.09·10^{-13}

From the influence of the temperature on CO_2 conversion, apparent activation energies (E_a) were calculated (Figure 4). The results show a variation of E_a values from 115±15 to 79±12 kJ×mol^{-1} depending on the nature of the Mo catalyst and its loading. These Ea values are in the range reported for other catalysts.[42,43]
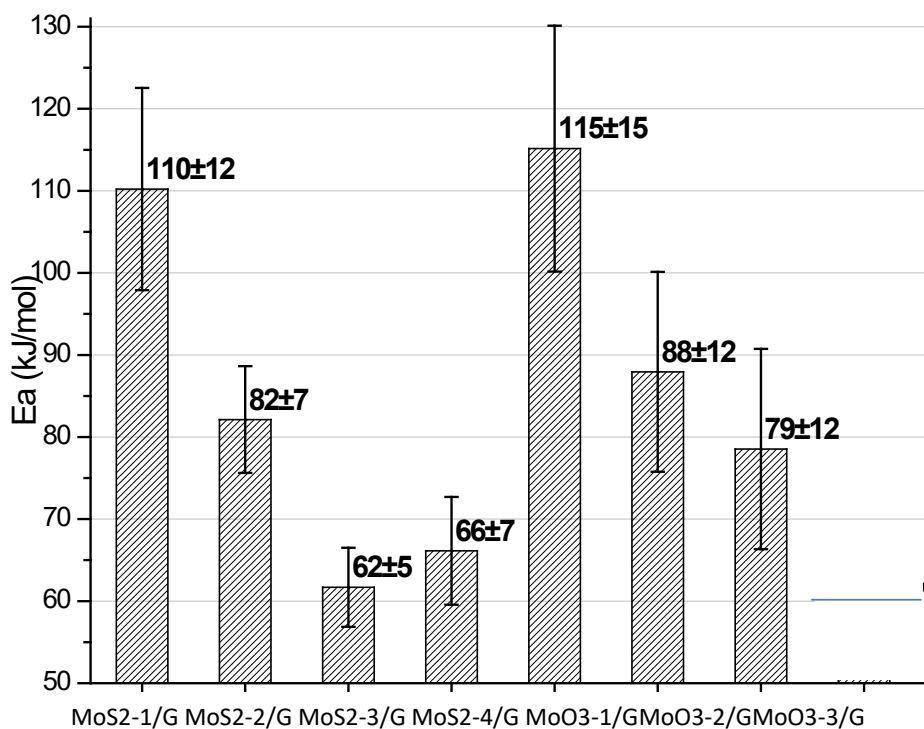

Figure 4. Comparison between the activation energy values for the methanation process in presence of the investigated graphene-based catalysts. The error bars are calculated from the standard deviation of the slope for each $\ln(CO_2$ conversion) vs. T^{-1} Arrhenius plot.

Catalyst stability was studied by carrying out a series of experiments in where under the same space velocity, the temperature of the reaction was increased from 300 to 500 °C and then, decreased again, observing in the case of MoO_3/G constantly reproducible catalytic data, while in the case of MoS_2/G some minor decay in activity upon time of stream was observed (Figure S6). XPS characterization of the samples before and after using the materials as catalysts for CO_2 hydrogenation showed no difference in the case of MoO_3/G, in agreement with the notable stability of these samples. In the case of MoS_2/G, some changes in the Mo 3d peak were observed in the MoS_2/G sample submitted to exhaustive use as catalyst in the CO_2 hydrogenation that are compatible with the formation of some Mo(VI) component in about 20 %. Figure 5 presents the XPS Mo 3d and O 1s peaks of the MoS_2/G sample fresh and after its use as CO_2 hydrogenation catalyst, where the remarkable changes in the shape and distribution of the O 1s peak can be seen, as well as the appearance in MO 3d of a component attributable to oxidized Mo^{VI}.[44-47] It should be commented at this point that also bulk MoS_2 is not completely stable under the reaction conditions according to XRD, where

the presence of some additional diffraction peaks after the use of the material as hydrogenation catalyst can be observed (see Figure S9 in the supporting information).
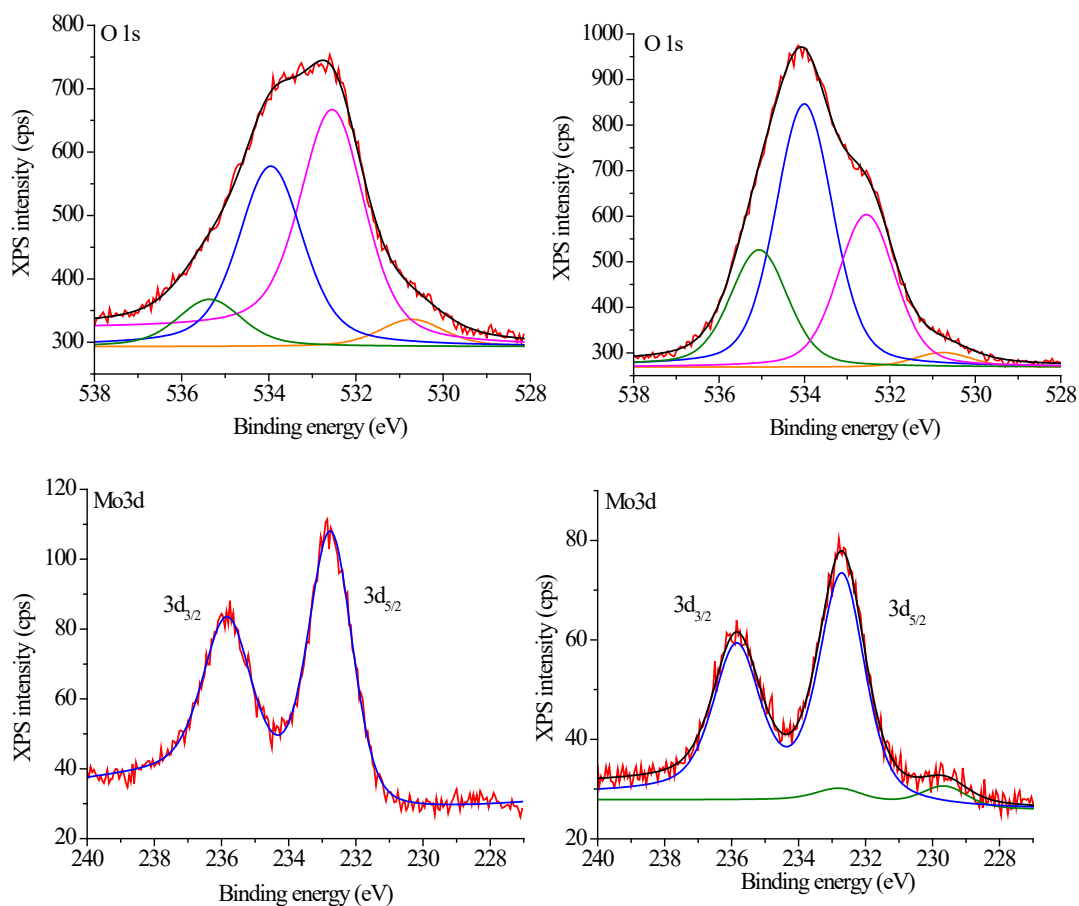

Figure 5. XPS O 1s and Mo 3d peaks of the MoS$_2$/G catalyst fresh (left) and after being exhaustively used as CO$_2$ hydrogenation catalysts (right).

Raman spectroscopy indicates that the changes in MoS$_2$ are most likely associated to the conversion of some MoS$_2$ in the corresponding MoO$_x$ oxide, based on the appearance of a new vibration band at 810 cm^{-1}.[48] Figure 6 illustrates these changes in the spent MoS$_2$/G respect to the fresh sample or even to the MoS$_2$/G exposed to CO$_2$ that should be responsible for oxidation of MoS$_2$, whereby the decrease or disappearance of the peaks associated to MoS$_2$ at 380, 407, 450, 590 and 630 cm^{-1} [49] are accompanied with the appearance of the characteristic MoOx band. Thus, it seems that the most likely cause of MoS$_2$/G instability is the partial reaction of MoS$_2$ with CO$_2$ causing some oxidation from Mo(IV) of MoS$_2$ to Mo(VI) and transformation to the oxide.
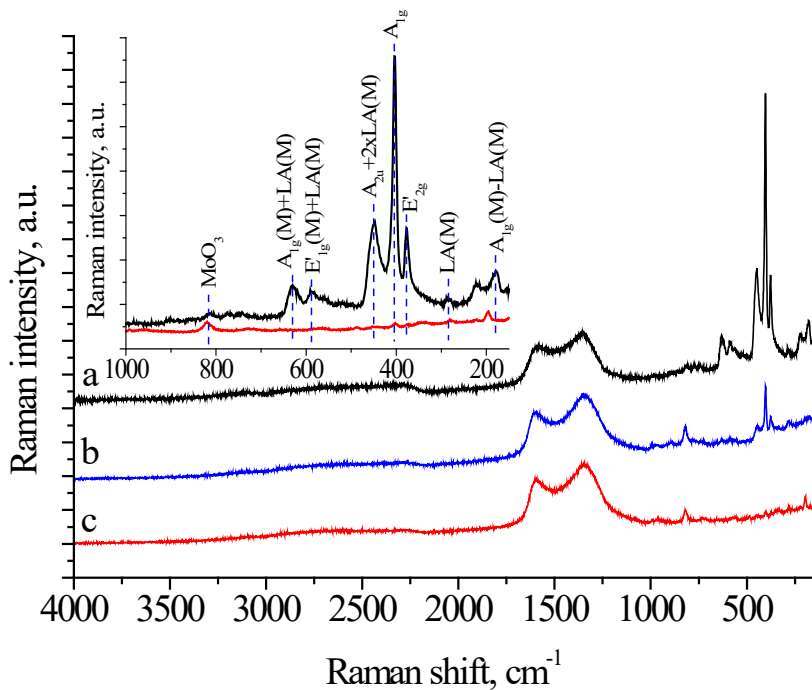
Figure 6. Raman spectra of the fresh MoS$_2$-2/G sample (a) and after being exposed to CO$_2$ at 500 °C (b) or after its extensive use as CO$_2$ hydrogenation catalyst (c). Inset: 1000-200cm^{-1} region for the fresh and spent sample.

Conclusions.

The present study has shown that MoS$_2$ supported on defective graphene derived from biomass is a selective catalysts for CO$_2$ methanation, increasing the catalytic activity with the temperature in the range from 300 to 600 °C. This catalytic activity sharply contrasts with that of bulk MoS$_2$ for which CO is the major product and reflects the important role of graphene on the activity of supported Mo species. There is an influence of the MoS$_2$ loading on graphene on the performance of the catalyst, there being an optimal MoO$_3$ exhibits a remarkable activity and stability, while MoS$_2$ undergoes some desulfuration under the reaction conditions and partial oxidation. It appears that the particle size is a critical parameter controlling the catalytic activity in the case of MoS$_2$/G prepared in a single pyrolysis step and that this limits the maximum loading of MoS$_2$ that can be deposited on the graphene. In the case of MoO$_3$ nanoparticles, their average particle size is not altered in the adsorption process and, consequently, higher loadings of 10 nm particles can be achieved, this resulting in an increasing catalytic activity as the loading increases in the range of 11 wt.%. The deposition of MoS$_2$ or MoO$_3$ onto graphene led to a different catalytic behavior compared to previously reported bulk catalysts, MoS$_2$ being more active than MoO$_3$. However, the methanation was almost complete on MoO$_3$/G compared to MoS$_2$/G on which part of the CO$_2$ was reduced only to CO. These results illustrate the potential of graphene as support of active molybdenum species in gas-phase hydrogenations.

References.

(1) Aresta, M. *Carbon dioxide as chemical feedstock*; John Wiley & Sons, 2010.

(2) Corma, A.; Garcia, H. Photocatalytic reduction of CO2 for fuel production: Possibilities and challenges. *Journal of catalysis* **2013,** *308*, 168.

(3) Huang, C.-H.; Tan, C.-S. A review: CO2 utilization. *Aerosol Air Qual. Res* **2014,** *14* (2), 480.

(4) Aresta, M.; Dibenedetto, A.; Angelini, A. The changing paradigm in CO2 utilization. *Journal of CO2 Utilization* **2013,** *3*, 65.

(5) Saeidi, S.; Amin, N. A. S.; Rahimpour, M. R. Hydrogenation of CO2 to value-added products—a review and potential future developments. *Journal of CO2 utilization* **2014,** *5*, 66.

(6) Arakawa, H. In *Studies in surface science and catalysis*; Elsevier, 1998; Vol. 114.

(7) Levene, J. I.; Mann, M. K.; Margolis, R. M.; Milbrandt, A. An analysis of hydrogen production from renewable electricity sources. *Solar Energy* **2007,** *81* (6), 773.

(8) Adamson, K.-A. Hydrogen from renewable resources—the hundred year commitment. *Energy Policy* **2004,** *32* (10), 1231.

(9) Beaudin, M.; Zareipour, H.; Schellenberglabe, A.; Rosehart, W. Energy storage for mitigating the variability of renewable electricity sources: An updated review. *Energy for sustainable development* **2010,** *14* (4), 302.

(10) Wang, W.; Wang, S.; Ma, X.; Gong, J. Recent advances in catalytic hydrogenation of carbon dioxide. *Chemical Society Reviews* **2011,** *40* (7), 3703.

(11) Federsel, C.; Jackstell, R.; Beller, M. State‐of‐the‐Art Catalysts for Hydrogenation of Carbon Dioxide. *Angewandte Chemie International Edition* **2010,** *49* (36), 6254.

(12) Bañares, M. A. Supported metal oxide and other catalysts for ethane conversion: a review. *Catalysis Today* **1999,** *51* (2), 319.

(13) Dhar, G. M.; Srinivas, B.; Rana, M.; Kumar, M.; Maity, S. Mixed oxide supported hydrodesulfurization catalysts—a review. *Catalysis Today* **2003,** *86* (1-4), 45.

(14) Volta, J.; Portefaix, J. Structure sensitivity of mild oxidation reactions on oxide catalysts-a review. *Applied catalysis* **1985,** *18* (1), 1.

(15) Grange, P.; Delmon, B. The role of cobalt and molybdenum sulphides in hydrodesulphurisation catalysts: A review. *Journal of the Less Common Metals* **1974,** *36* (1-2), 353.

(16) Zaman, S.; Smith, K. J. A review of molybdenum catalysts for synthesis gas conversion to alcohols: catalysts, mechanisms and kinetics. *Catalysis Reviews* **2012,** *54* (1), 41.

(17) Meng, F.; Li, J.; Cushing, S. K.; Zhi, M.; Wu, N. Solar hydrogen generation by nanoscale p–n junction of p-type molybdenum disulfide/n-type nitrogen-doped reduced graphene oxide. *Journal of the American Chemical Society* **2013,** *135* (28), 10286.

(18) Liu, Y.; Wu, H.; Cheng, H.-C.; Yang, S.; Zhu, E.; He, Q.; Ding, M.; Li, D.; Guo, J.; Weiss, N. O. Toward barrier free contact to molybdenum disulfide using graphene electrodes. *Nano letters* **2015,** *15* (5), 3030.

(19) Saito, M.; Anderson, R. B. The activity of several molybdenum compounds for the methanation of CO2. *Journal of catalysis* **1981,** *67* (2), 296.

(20) Yao, S.; Gu, L.; Sun, C.; Li, J.; Shen, W. Combined methane co2 reforming and dehydroaromatization for enhancing the catalyst stability. *Industrial & Engineering Chemistry Research* **2008,** *48* (2), 713.

(21) Li, H.; Wang, L.; Dai, Y.; Pu, Z.; Lao, Z.; Chen, Y.; Wang, M.; Zheng, X.; Zhu, J.; Zhang, W.et al. Synergetic interaction between neighbouring platinum monomers in CO2 hydrogenation. *Nature Nanotechnology* **2018,** *13* (5), 411.

(22) Liu, P.; Choi, Y.; Yang, Y.; White, M. G. Methanol synthesis from H2 and CO2 on a Mo6S8 cluster: a density functional study. *The Journal of Physical Chemistry A* **2009,** *114* (11), 3888.

(23) Huang, M.; Cho, K. Density Functional Theory Study of CO Hydrogenation on a MoS2 Surface. *The Journal of Physical Chemistry C* **2009,** *113* (13), 5238.

(24) Liu, X.; Song, Y.; Geng, W.; Li, H.; Xiao, L.; Wu, W. Cu-Mo2C/MCM-41: An efficient catalyst for the selective synthesis of methanol from CO2. *Catalysts* **2016,** *6* (5), 75.

(25) Posada-Pérez, S.; Ramírez, P. J.; Evans, J.; Viñes, F.; Liu, P.; Illas, F.; Rodriguez, J. A. Highly active Au/δ-MoC and Cu/δ-MoC catalysts for the conversion of CO2: The metal/C ratio as a key factor defining activity, selectivity, and stability. *Journal of the American Chemical Society* **2016,** *138* (26), 8269.

(26) Shi, Y.; Yang, Y.; Li, Y.-W.; Jiao, H. Activation mechanisms of H2, O2, H2O, CO2, CO, CH4 and C2Hx on metallic Mo2C (001) as well as Mo/C terminated Mo2C (101) from density functional theory computations. *Applied Catalysis A: General* **2016,** *524*, 223.

(27) Porosoff, M. D.; Baldwin, J. W.; Peng, X.; Mpourmpakis, G.; Willauer, H. D. Potassium‐Promoted Molybdenum Carbide as a Highly Active and Selective Catalyst for CO2 Conversion to CO. *ChemSusChem* **2017,** *10* (11), 2408.

(28) Li, N.; Chen, X.; Ong, W.-J.; MacFarlane, D. R.; Zhao, X.; Cheetham, A. K.; Sun, C. Understanding of Electrochemical Mechanisms for CO2 Capture and Conversion into Hydrocarbon Fuels in Transition-Metal Carbides (MXenes). *ACS nano* **2017,** *11* (11), 10825.

(29) Latorre-Sánchez, M.; Esteve-Adell, I.; Primo, A.; García, H. Innovative preparation of MoS2–graphene heterostructures based on alginate containing (NH4) 2MoS4 and their photocatalytic activity for H2 generation. *Carbon* **2015,** *81*, 587.

(30) He, J.; Fernández, C.; Primo, A.; Garcia, H. One-Step Preparation of Large Area Films of Oriented MoS2 Nanoparticles on Multilayer Graphene and Its Electrocatalytic Activity for Hydrogen Evolution. *Materials* **2018,** *11* (1), 168.

(31) Poling, B. E.; Prausnitz, J. M.; O'connell, J. P. *The properties of gases and liquids*; Mcgraw-hill New York, 2001.

(32) Green, D. W. *Perry's chemical engineers'*; McGraw Hill, 2008.

(33) Vannice, M. A.; Joyce, W. H. *Kinetics of catalytic reactions*; Springer, 2005.

(34) Fogler, H. S. Elements of chemical reaction engineering. **1999**.

(35) Dhakshinamoorthy, A.; Primo, A.; Concepcion, P.; Alvaro, M.; Garcia, H. Doped Graphene as a Metal‐Free Carbocatalyst for the Selective Aerobic Oxidation of Benzylic Hydrocarbons, Cyclooctane and Styrene. *Chemistry-A European Journal* **2013,** *19* (23), 7547.

(36) Trandafir, M. M.; Florea, M.; Neaţu, F.; Primo, A.; Parvulescu, V. I.; García, H. Graphene from Alginate Pyrolysis as a Metal‐Free Catalyst for Hydrogenation of Nitro Compounds. *ChemSusChem* **2016,** *9* (13), 1565.

(37) Xie, J.; Zhang, H.; Li, S.; Wang, R.; Sun, X.; Zhou, M.; Zhou, J.; Lou, X. W. D.; Xie, Y. Defect‐rich MoS2 ultrathin nanosheets with additional active edge sites for enhanced electrocatalytic hydrogen evolution. *Advanced materials* **2013,** *25* (40), 5807.

(38) Gao, Y.; Ma, D.; Wang, C.; Guan, J.; Bao, X. Reduced graphene oxide as a catalyst for hydrogenation of nitrobenzene at room temperature. *Chemical Communications* **2011,** *47* (8), 2432.

(39) Hu, H.; Xin, J. H.; Hu, H.; Wang, X.; Kong, Y. Metal-free graphene-based catalyst—Insight into the catalytic activity: A short review. *Applied Catalysis A: General* **2015,** *492*, 1.

(40) Primo, A.; Neatu, F.; Florea, M.; Parvulescu, V.; Garcia, H. Graphenes in the absence of metals as carbocatalysts for selective acetylene hydrogenation and alkene hydrogenation. *Nature communications* **2014,** *5*, 5291.

(41) Missen, R. W.; Mims, C. A.; Saville, B. A. *Introduction to chemical reaction engineering and kinetics*; Wiley New York, 1999.

(42) Weatherbee, G. D.; Bartholomew, C. H. Hydrogenation of CO2 on group VIII metals: II. Kinetics and mechanism of CO2 hydrogenation on nickel. *Journal of Catalysis* **1982,** *77* (2), 460.

(43) Weatherbee, G. D.; Bartholomew, C. H. Hydrogenation of CO2 on group VIII metals: I. Specific activity of NiSiO2. *Journal of Catalysis* **1981,** *68* (1), 67.

(44) Haber, J.; Machej, T.; Ungier, L.; Ziółkowski, J. ESCA studies of copper oxides and copper molybdates. *Journal of Solid State Chemistry* **1978,** *25* (3), 207.

(45) Smith, M.; Ozkan, U. The partial oxidation of methane to formaldehyde: role of different crystal planes of MoO3. *Journal of Catalysis* **1993,** *141* (1), 124.

(46) Wei, J.; Yin, Z.; Chen, S.-C.; Cai, D.; Zheng, Q. Solution-processed MoS x thin-films as hole-transport layers for efficient polymer solar cells. *RSC Advances* **2016,** *6* (45), 39137.

(47) Brox, B.; Olefjord, I. ESCA studies of MoO2 and MoO3. *Surface and interface analysis* **1988,** *13* (1), 3.

(48) Dieterle, M.; Mestl, G. Raman spectroscopy of molybdenum oxides Part II. Resonance Raman spectroscopic characterization of the molybdenum oxides Mo 4 O 11 and MoO 2. *Physical Chemistry Chemical Physics* **2002,** *4* (5), 822.

(49)   Gołasa, K.; Grzeszczyk, M.; Korona, K.; Bożek, R.; Binder, J.; Szczytko, J.; Wysmołek, A.; Babiński, A. Optical Properties of Molybdenum Disulfide (MoS 2). *Acta Physica Polonica, A.* **2013,** *124* (5).